AIAA JOURNAL
Vol. 47, No. 7, July 2009

Measurements of Flow Around a Flap Side Edge with Porous Edge Treatment

D. Angland* and X. Zhang†
University of Southampton, Southampton SO17 1BJ, United Kingdom
and
N. Molin‡
Airbus, 31060 Toulouse, France

DOI: 10.2514/1.39311

Wind-tunnel experiments were performed to investigate a flap side-edge vortex, which is a contributor to airframe noise. The flowfield investigation showed that the peak turbulent stresses were contained in the shear layer that rolled up to form the flap side-edge vortex. The wake from the main element was also entrained by the side-edge vortex. The near-field pressure fluctuations where the turbulent shear layer impinged on the flap side edge were broadband in nature from a Strouhal number of 10 to 50. Hot-wire measurements on the downstream vortex identified a broadband instability centered around a Strouhal number of 13.2. A porous side-edge treatment was applied to the half-span flap to modify the flap side-edge flowfield. The effect of applying a porous side edge was to reduce the Reynolds stresses contained within the vortex and the shear layer that formed it. The porous material also had the effect of displacing the vortex further away from the flap surface. This led to a reduction in the broadband pressure perturbations measured at the flap side edge. Compared with the accuracy of the measurements of the aerodynamic forces, the aerodynamic impact of the porous flap side edge was almost negligible.

Nomenclature

b	=	span of flap, m
C	=	interial loss factor, 1/m
c	=	reference chord, m
C_D	=	drag coefficient
c_F	=	flap chord, m
C_L	=	lift coefficient
$E(f)$	=	power spectral density, m^2/s
n	=	thickness of porous material, m
St_F	=	Strouhal number based on flap chord
t	=	maximum thickness of flap, m
u, v, w	=	Cartesian components of velocity vector, m/s
v_j	=	permeation velocity through porous material, m/s
V_∞	=	freestream velocity, m/s
x, y, z	=	Cartesian coordinates, x positive downstream, y positive up, z positive to port
x_F	=	distance along flap chord, m
α	=	main element angle of attack, deg
α_v	=	viscous loss factor, m^2
Δp	=	pressure loss across porous material, N/m^2
δ_F	=	flap deflection angle, deg
μ	=	viscosity, $N \cdot s/m^2$
ρ	=	density, kg/m^3
Ω	=	nondimensional vorticity

Presented as Paper 213 at the 44th AIAA Aerospace Sciences Meeting and Exhibit, Reno, NV, 9–12 January 2006; received 7 July 2008; revision received 20 February 2009; accepted for publication 15 February 2009.

*Ph.D. Student, School of Engineering Sciences.
†Professor, School of Engineering Sciences. Associate Fellow AIAA.
‡Ph.D. Engineer, Acoustic and Environment Department, 316 Route de Bayonne, PO Box M0112/4, Cedex 03.

I. Introduction

With civil aviation noise regulations becoming more stringent, airframe noise is an important consideration for civil aircraft manufacturers. Noise of modern aircraft in their approach configuration can be dominated by airframe noise because the engines are normally operated at a reduced power setting. The main contributors to airframe noise are landing gears and high-lift devices.

Experimental studies were performed over 20 years ago that showed strong airframe noise associated with the side edge of a deployed flap [1–3]. Attempts have been made to model the mechanism responsible for noise generation at a flap side edge [4–6]. More recent experimental work has been aimed at understanding and describing the mechanism responsible for flap side-edge noise [7–9]. Various three-dimensional steady Reynolds-averaged Navier–Stokes (RANS) computations have also identified the major flow physics present in the flap side-edge region [10–12].

Choudhari and Khorrami [13] performed a computational study of a porous flap side edge as a passive means of flap noise reduction. Because the near-field unsteadiness was not modeled, it was not possible to translate the flow alterations into accompanying reductions in sound pressure level (SPL). Previous experimental work [14] had achieved noise reduction by replacing a part of the flap side edge with brushes and an open cell porous edge. A noise reduction of up to 4 dB in the far field was reported, within a limited band of frequencies. The physics responsible for this noise reduction were not discussed. Revell et al. [15] performed a series of experiments investigating a porous acoustic treatment applied to a trailing-edge flap. Phased microphone array measurements were used to determine the reduction achieved. The mechanisms proposed for the reduction of flap side-edge noise were dissipation and modification of the vortex. The mean flow was modified due to the permeation velocity through the porous material, which interfered with the fluctuating vortex causing some cancellation. The porous material also had a damping effect on the pressure fluctuations due to its finite impedance. Various other noise reduction methods have been applied to the flap side-edge problem such as continuous mold-line technology [16], active flow control [17], and flap fences [18–22].

Macaraeg [7] found that the shear layer instabilities in the flap side-edge flowfield were broadband in nature from 5 to 30 kHz. The

lower frequencies were dominated by vortex instabilities. Brooks and Humphreys [9] performed experiments at a Reynolds number of 1.7×10^6 and hypothesized a shear layer instability model for noise production. Choudhari et al. [23] found the strongest coherence between microphones from 1500 to 4000 Hz. A 5 kHz source was determined to be the interaction between the vortex and the flap trailing edge. Koop and Ehrenfried [17] found flap side-edge noise dominated at a Strouhal number based on a flap chord of approximately 12.6, similar to the result of Choudhari et al. [23]. The use of active and passive flow control methods for noise reduction were investigated at a Reynolds number of 1.14×10^6. The reduction with blowing was in the frequency range $2.5 \leqslant f \leqslant 5$ kHz. Dobrzynski et al. [24] found a tone on scale flap side-edge tests that existed at a Strouhal number based on a flap chord (St_F) of 6.0 that did not exist at full scale. It was hypothesized that this was due to laminar flow separation at the flap side edge.

The hydrodynamic perturbations responsible for the sound radiated by a flap side edge pose a challenge to numerical modelling. The flap side-edge flowfield is a fully three-dimensional, time-dependent turbulent flow with large disparities in temporal and spatial scales. The unsteady flowfield is driven by nonlinearities in the inertial and diffusion terms in the Navier–Stokes equations. These experiments, performed on a generic, simplified model, provide an insight into the aeroacoustics and aerodynamics of a flap side edge and the effect of the application of a porous flap side edge. A variety of experimental techniques were employed to understand the mechanism by which the application of a porous flap side edge reduced the noise.

II. Experimental Apparatus and Procedure

A. Wind Tunnel

The experiments were conducted in the University of Southampton's 3.5×2.5 m wind tunnel. The tunnel was a closed circuit return type with a closed working section. The freestream turbulence level was less than 0.3% at 30 m/s. The wind tunnel incorporated a chiller that maintained the air temperature at 19 °C.

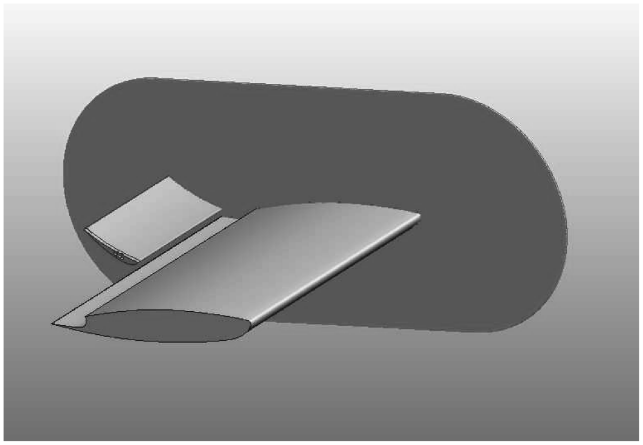

Fig. 1 Wind-tunnel model with port side endplate removed. Flow is from right to left.

B. Model Design and Test Configuration

The wing used in the experiments was of a high-lift design with a fixed leading edge and a half-span trailing-edge flap, shown in Fig. 1. The origin of the axis system was at the leading edge of the main element in the $x - y$ plane and at the flap side edge in the z direction as depicted in Fig. 2. The chord of the main element was 0.71 m and the span was 1 m. The chord and span of the trailing-edge flap were 0.198 and 0.5 m, respectively. The maximum thickness of the flap was 0.021 m. The reference length, based on the retracted chord of the model, was 0.8 m. The reference planform area used in the calculation of the force coefficients was 0.8 m^2. The main element was machined from wood, and the half-span flap was made from carbon-fibre skins and machined aluminum ribs. The range of Reynolds numbers tested were 0.6×10^6 to 2.0×10^6, based on the reference length. The angle of attack range was 0 to 15 deg, and the flap deflection range was 29 to 39 deg. Measurements conducted included forces, particle image velocimetry (PIV), hot-wire anemometry, and on-surface microphones.

C. Porous Flap Side Edge

Experiments were performed with a hard wall and a porous flap side edge with three different porosities that are tabulated in Table 1. The porous material used was a Duocel open cell aluminum foam shown in Fig. 3.

The material properties were defined in terms of porosity measured in pores per inch (PPI) and relative density. The relative density was defined as the ratio of the density of the porous material to the density of the base metal. The porous treatment was applied to the outboard 0.02 m of the flap, which corresponded to 4% of the span of the flap. This spanwise extent of the porous side-edge treatment was the same as in the computational study by Choudhari and Khorrami [13]. The pressure drop across a porous material (Δp) is a function of the permeation velocity through the material (v_j). It comprises a viscous loss term and an inertial loss term [25]:

$$\frac{\Delta p}{\Delta n} = \frac{\mu}{\alpha_v} v_j + \frac{1}{2} \rho C v_j^2 \tag{1}$$

where Δn is the thickness of the porous material, α_v is the permeability constant, and C is the inertial resistance factor. A second-order polynomial curve was fitted to flow resistance data from the supplier [26] to determine the constants in Eq. (1). An example is given in Fig. 4. The viscous loss and inertial loss terms are tabulated in Table 1 for each of the three materials tested.

D. Forces

The wind tunnel contained a six-component balance with Nutem load cells. Only lift and drag data are presented in the results section. The accuracy of the lift and drag load cells was within 0.03% of the full range. The interaction terms between the force components measured were accounted for in the calibration of the balance.

The angle of attack of the main element was set to ± 0.05 deg. The freestream values of temperature, static pressure, and velocity were averaged from the values at the beginning and the end of each run. The average variations between the start and the end of the run were ± 0.5°C for temperature, ± 0.1 mm H_2O for pressure, and ± 0.01 m/s for velocity. The force measurements were averaged over three runs. The uncertainty of the force coefficient C_L varied with angle of attack. The standard mean error was calculated for three

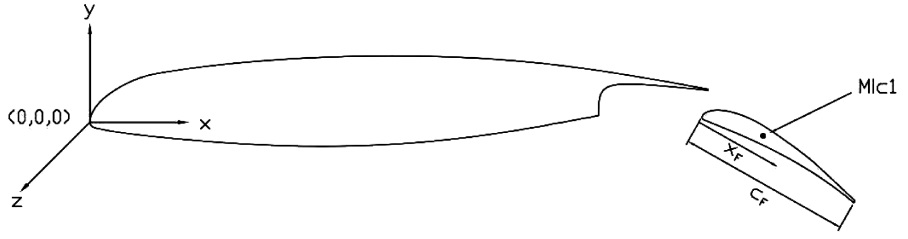

Fig. 2 Geometry showing the definition of axes and location of microphone. Flow is from left to right.

Table 1 Porous materials properties

Porosity, PPI	Relative density, %	$1/\alpha_v$, $1/m^2$	C, $1/m$
20	5–7	3.824×10^7	549.05
40	5–7	5.076×10^7	883.53
40	10–12	7.509×10^7	1067.28

runs within 95% confidence limits. The largest uncertainty was at an angle of attack of 20 deg and was equal to $C_L \pm 0.004$. The largest uncertainty of the drag coefficient was $C_D \pm 0.002$ at 20 deg. The force coefficients were corrected for blockage effects using a quasi-streamlined method [27]. The correction is appropriate for bodies with separated flow. The coefficient corrections were calculated for each angle of attack that was measured.

E. Particle Image Velocimetry

The fluid was seeded with particles typically in the range 1 to 5 μm for the purpose of PIV measurements. The seeding particles in the plane of interest were illuminated with two Gemini Nd:YAG lasers that were capable of running at 4 Hz, emitting 120 mJ pulses at 532 nm. The positions of these particles were recorded on a charge-coupled device digital camera at two different times, 10–30 μs apart, depending on airspeed. The typical laser sheet thickness was 2–3 mm.

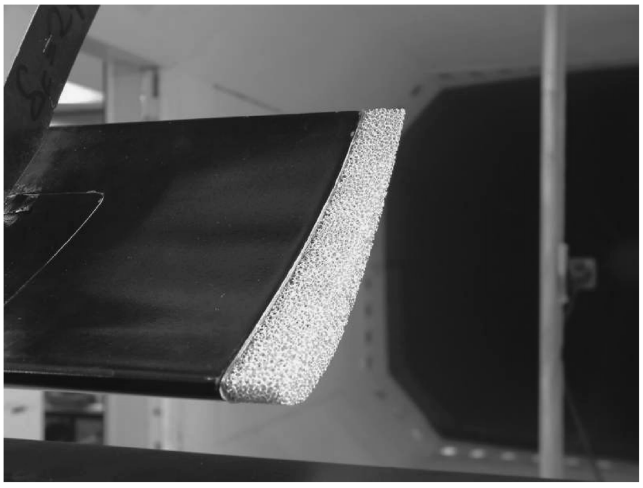

Fig. 3 A downstream view of the porous flap side edge. The PIV camera can be seen mounted on the strut in the background. The laser sheet shines from right to left in a vertical plane.

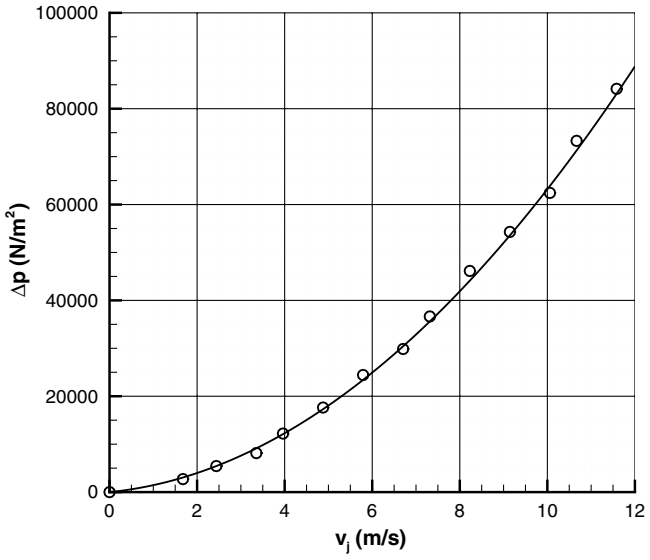

Fig. 4 Second-order polynomial fit with flow resistance data [26] for 40 PPI 5–7% porous material.

The laser sheet was shined in a vertical plane through a glass window, which made up the port wall of the working section and then through a second glass window that formed part of the endplate. The laser was mounted on a one-dimensional traverse that was placed parallel to the mean flow direction so that it could easily be moved from one plane to another. The camera was attached to a strut, which was mounted from the floor to the ceiling of the wind tunnel approximately 10 chord lengths downstream of the model. This allowed $y - z$ planes through the vortex core to be examined. The smoke generator was placed aft of the working section of the wind tunnel. This ensured the smoke had sufficiently diffused to ensure homogeneity in seeding levels by the time the smoke reached the model.

An adaptive cross correlation was performed up to a final interrogation area measuring 16×16 pixels. The horizontal and vertical overlap was 75%. A peak validation of 1.2 was used to reject spurious vectors. The peak validation is the ratio of the first peak in the correlation plane to the second and is a measure of the signal-to-noise ratio. These time-averaged data were averaged over 300 images sampled at 2 Hz. The physical resolution of the generated vector map was 1.2×10^{-3} m in both directions. The standard error of the mean components of velocity, within 95% confidence limits, was ± 0.01 m/s for 300 samples.

F. Hot-Wire Anemometry

A single 5 μm tungsten hot wire was used to determine the spectral content of the vortex. The hot-wire probe was placed on a one-dimensional traverse placed vertically, which allowed the hot wire to traverse through the vortex core. The hot wire was calibrated in freestream using a pitot-static tube connected to a digital micromanometer. The calibration was performed from 0 to 36 m/s in steps of 3 m/s. The average error in the hot wire for the calibration run was 0.32%. The hot wire signal was sampled at 20 kHz. A fast Fourier transform (FFT) with a Hanning window function was performed on the hot-wire signal to obtain the spectral content of the flow. The FFT was averaged over 50 blocks. Each block contained 16,384 samples. The frequency resolution was 1.2 Hz.

G. Microphones' Measurements

The microphones used were Panasonic WM-60A omnidirectional condenser microphones. These were flush mounted onto the surface of the model. The sensitivity was -44 ± 5 dB (0 dB = 1 V/Pa at 1 kHz). The measurable frequency range was from 20 to 20 kHz. The operating voltage was 2 V provided by a preamp, and the signal-to-noise ratio was greater than 58 dB. The typical frequency response curve, supplied by the manufacturer, showed that the relative response was constant across the frequency range. The signal from the microphone was sampled at 44 kHz for 10 s. An FFT was performed with a Hanning window function. The FFT size was 8192 and was averaged over 54 blocks. The frequency resolution of the spectrum was 5 Hz.

III. Results and Discussion

A. Aerodynamic Forces

Force measurements were taken with three different porous treatments applied to the side edge to determine the aerodynamic penalty associated with their use. The porous flap side edge could not support a pressure difference without allowing a finite transpiration velocity through the material. An important parameter to determine was the aerodynamic effect of applying a porous side edge to the flap. The use of porous materials to modify the flap side-edge vortex was of little practical benefit if there was a large aerodynamic penalty associated with its use.

The lift and drag were measured at three different Reynolds numbers, 0.7×10^6, 1.3×10^6, and 2.0×10^6. Eleven angles of attack were measured ranging from -5 to 20 deg in steps of 2.5 deg.

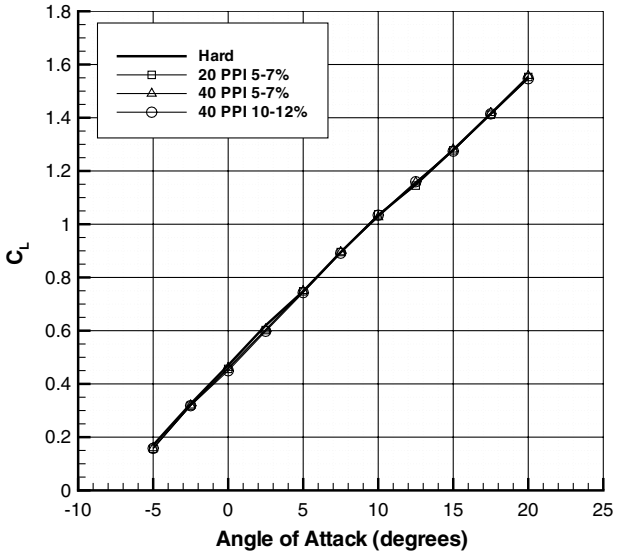

a) C_L

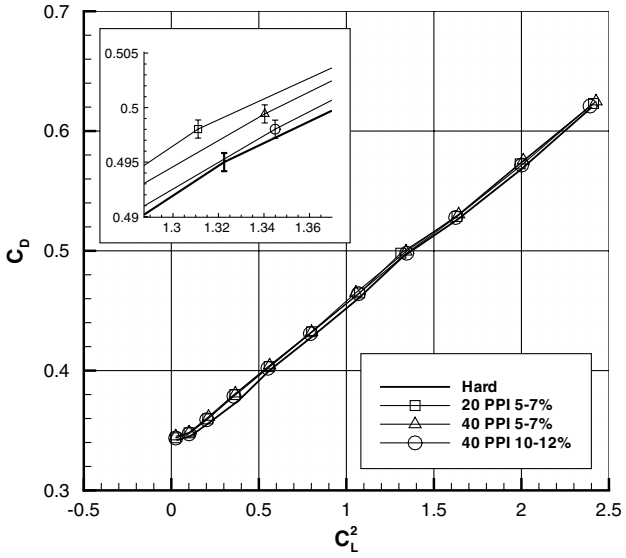

b) C_D

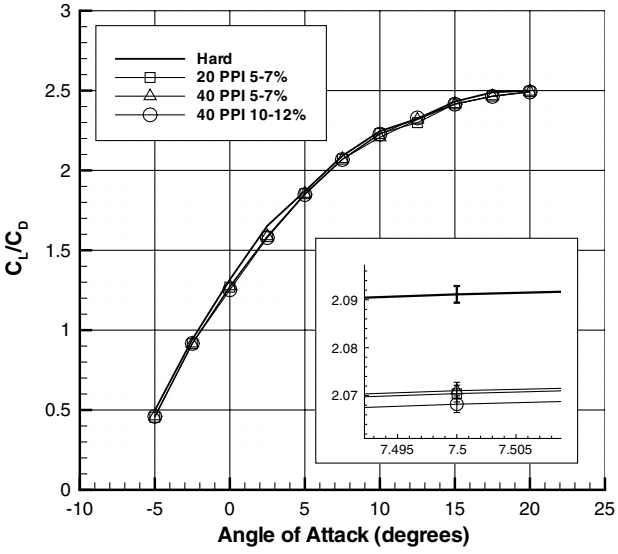

c) C_L/C_D

Fig. 5 Aerodynamic forces with porous materials applied.

The lift curves for the three porous treatments and for the hard-wall case are shown in Fig. 5a. These data were at a Reynolds number of 2.0×10^6. The application of the porous material 20 PPI 5–7% resulted in a reduction of C_L of 0.005 ± 0.004 averaged over the angle-of-attack range. The reduction in the lift force was diminutive and was close to the uncertainty of the experiments. The C_L with a treatment of 40 PPI 5–7% was 0.002 ± 0.005 lower than the hard-wall case. The final porous treatment was the least permeable with a porosity of 40 PPI and a relative density of 10–12%. The lift coefficient was 0.007 ± 0.006 less than the hard-wall case. Compared with the accuracy of the lift forces, the aerodynamic impact on the lift forces of the porous side edge was negligible.

The application of a porous flap side edge had a slight increase in drag. The drag plotted against lift squared is shown in Fig. 5b. At a Reynolds number of 2.0×10^6, the C_D with a porous side edge of 20 PPI 5–7% was 0.0034 ± 0.0006 greater than the hard-wall values averaged over the angle-of-attack range. The C_D was 0.0046 ± 0.0006 greater than the hard-wall values for the 40 PPI 5–7% porous case. The drag coefficient was 0.024 ± 0.0006 greater than the hard-wall case for the least permeable porous side edge (40 PPI 10–12%). A close up of the error bars in the drag measurement are shown in the inset in Fig. 5b at an angle of attack of 7.5 deg (a typical approach angle of attack).

The aerodynamic efficiency (C_L/C_D) is shown in Fig. 5c for a Reynolds number of 2.0×10^6. The loss in aerodynamic efficiency for each of the porous materials was 0.028 ± 0.01 averaged over the angle-of-attack range. An inset in Fig. 5c shows the error bars at an angle of attack of 7.5 deg. The reduction in aerodynamic efficiency corresponded to approximately 1.1% averaged over the entire angle of attack range. The reduction in efficiency was due to the increased drag due to the nature of the porous material. The flow through the porous material resulted in a pressure loss across the material, which produced a net drag force. Compared with the accuracy of the measurements of the aerodynamic forces, the aerodynamic impact of the porous side edge was small.

The lift curves were insensitive to the Reynolds number, as shown in Fig. 6a. The drag curves, shown in Fig. 6b, had a slight dependency on Reynolds number. The flap had a small region of separated flow toward the trailing edge, as will be discussed in the surface flow visualization results. The position of this separation line had a slight dependence on Reynolds number over the range measured. The higher the Reynolds number, the further aft along the flap chord the separation occurred. This resulted in a slight reduction in the wake size, which resulted in a small reduction in drag. Increasing the Reynolds number from 0.7×10^6 to 2.0×10^7 resulted in a reduction in C_D of 0.019, averaged over the angle-of-attack range.

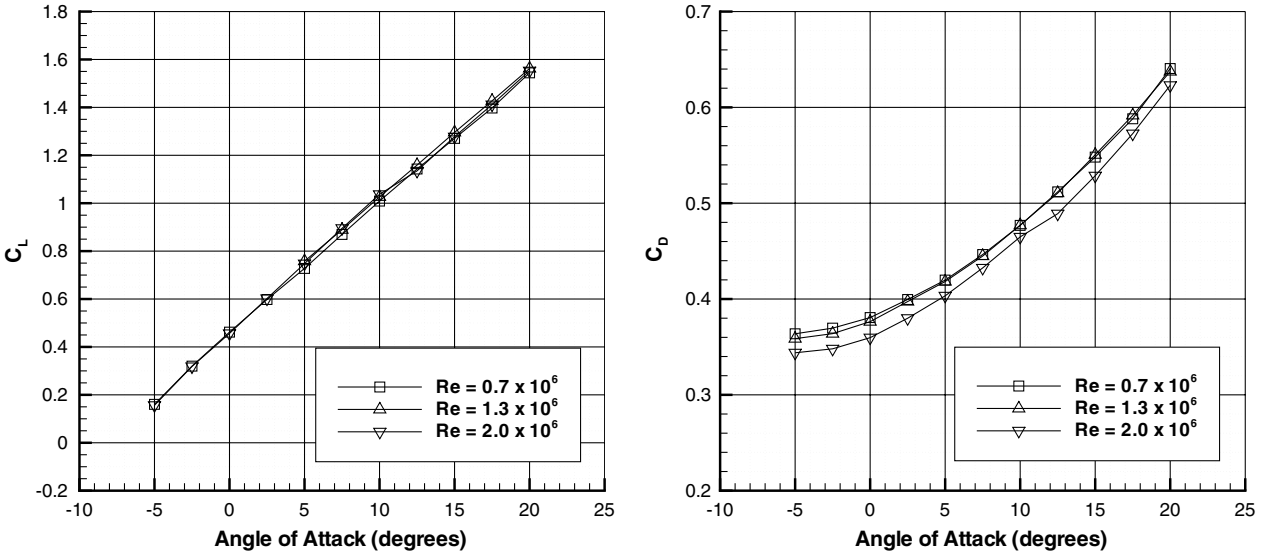

a) Lift with 20 PPI 5 - 7%

b) Drag with 20 PPI 5 - 7%

Fig. 6 Effect of Reynolds number on aerodynamic forces.

B. Surface Flow Visualization

Near the leading edge of the flap, evidence of a dual vortex system can be seen. McInerny et al. [28] provided a description of this dual vortex system for a blunt-tipped airfoil. It has also been reported previously in experimental and computational studies related to flap side-edge noise [8,11,12]. In this study the surface flow visualization was useful in determining the appropriate location of pressure transducers and to relate near-field measurements to flow features for this simplified model.

A shear layer separated from the pressure surface of the flap and reattached along the primary attachment line, shown in Fig. 7. Because of the sharp edge, the separation line was fixed at the bottom edge. The roll up of this shear layer formed a vortex. At the upper edge of the flap a secondary vortex separated from the sharp edge and reattached on the suction surface of the flap on the secondary vortex reattachment line, as indicated in Fig. 8. The main vortex grew rapidly in size in the streamwise direction as evidenced by the primary attachment line moving toward the suction surface of the flap side edge. At the primary attachment line, the flow bifurcated toward the suction and pressure surfaces. The flow above the primary attachment line separated from the upper edge to form the secondary vortex, which reattached on the suction surface of the flap. The flow on the lower half on the primary attachment line separated at the secondary separation line before it reached the lower edge. This is shown in the schematic in Fig. 9. This formed a small region of recirculation that grew slowly in the streamwise direction just above the lower edge of the flap. As the vortices on the side edge and upper surface merged, they separated from the flap surface. A focal point was situated on the edge between the side edge and the suction surface of the flap at approximately two-thirds of the flap chord. This was evidenced by an accumulation of oil during the run. Downstream of this focal point the flow was reversed, as seen in Fig. 8, and the vortex was detached from the surface. The location of this focal point differed from the computational study performed by Khorrami et al. [10,11] where it was located on the side edge. The change in location was due to the trajectory of the flap side-edge vortex and where it detached from the surface of the flap.

C. Vortex Formation and Evolution

1. Hard Wall

The near-field formation and evolution of the vortex was examined using PIV. The near-field flow structures were determined and related to potential acoustic sources. Similar mean flow features were found by other authors as mentioned in the preceding section. Further flowfield details, including the Reynolds stresses, were provided by these measurements as well as providing a baseline for the porous flap side-edge measurements.

The nondimensional vorticity at PIV plane 1 ($x_F/c_F = 0.2$) is shown in Fig. 10a for the hard-wall case. The vorticity was nondimensionalized with the flap chord and the freestream velocity.

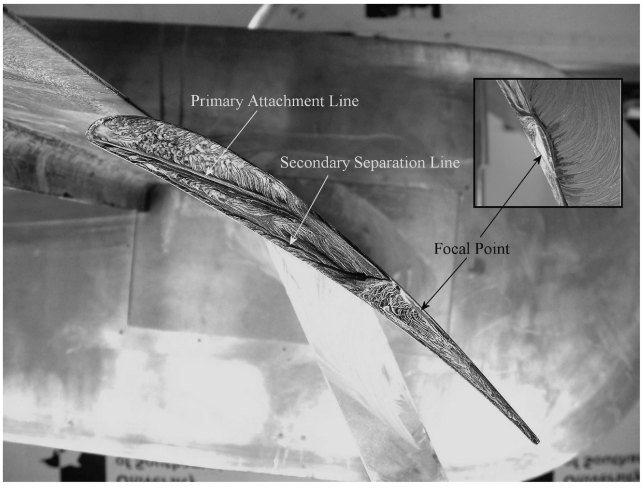

Fig. 7 Oil flow of flap side edge showing major flow features. View looking starboard, flow is from left to right.

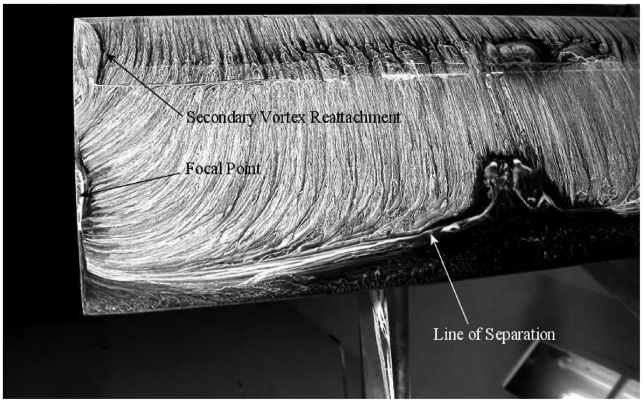

Fig. 8 Oil flow of suction surface of flap. View looking upstream.

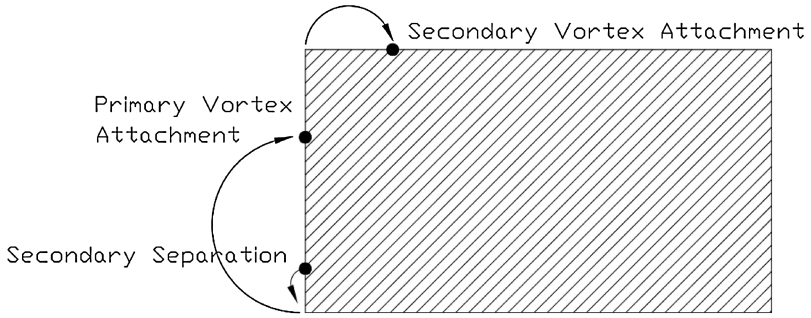

Fig. 9 Schematic of flap side-edge flow in $y-z$ plane at $x_F/c_F = 0.27$. View looking upstream.

The vorticity was defined as follows in terms of the coordinate system shown in Fig. 2:

$$\Omega = \frac{(\frac{\partial w}{\partial y} - \frac{\partial v}{\partial z})c_F}{V_\infty} \tag{2}$$

The vorticity plot showed the presence of a dual vortex system with a primary vortex attaching on the flap side edge and a significantly weaker vortex on the flap suction surface. Above the suction surface of the flap, at approximately $y/t_F = 1.4$, there was a small band of vorticity. This band of vorticity was in close proximity to the trailing edge of the main element shown as a dotted line in Fig. 10a. The source of this vorticity was presumed to be the wake of the main element, which was convected through the gap between the trailing edge of the main element and the suction surface of the flap. The deflection of this main element wake vorticity due to the presence of the vortex was minimal at this plane because the strength of the vortex was small.

A profile of the vertical velocity component v is shown in Fig. 11a at $y/t_F = -0.375$ at PIV plane 1. The peak velocity across this profile is as at the edge of the vortex. A shear layer that originated from the separated flow from the pressure surface of the flap was wrapped around the vortex. The turbulent stress profile at this plane was also examined to determine potential acoustic sources (Fig. 11b). The peak stress ($v'v'$) is contained in the shear layer. This shear layer was wrapped around the vortex and impinged on the flap side edge. An on-surface microphone was placed at the attachment line to determine the pressure perturbations produced when this turbulent shear layer impinged on the flap side edge on the primary attachment line.

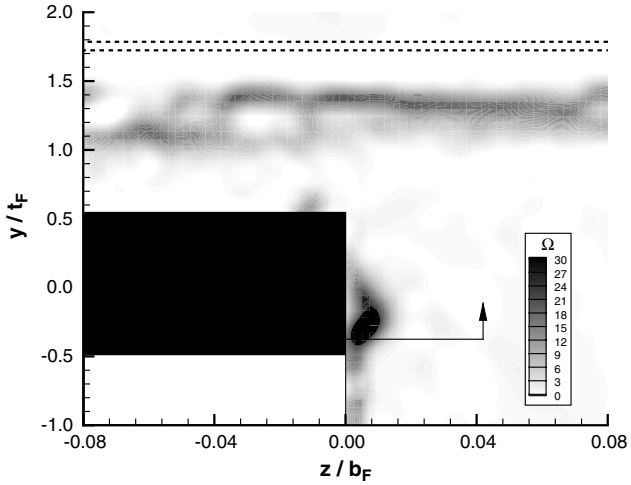

a) PIV plane 1 ($x_F/c_F = 0.2$)

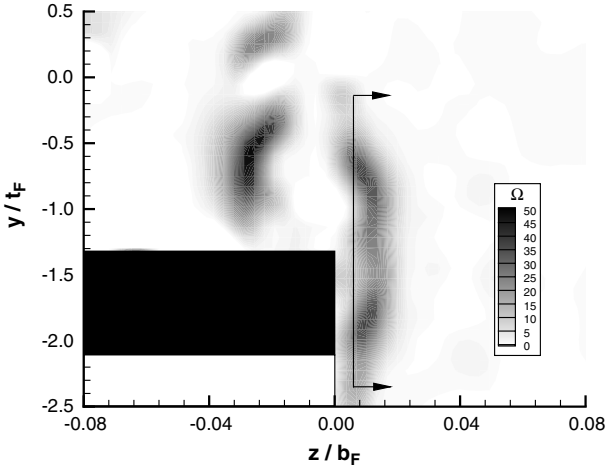

b) PIV plane 2 ($x_F/c_F = 0.6$)

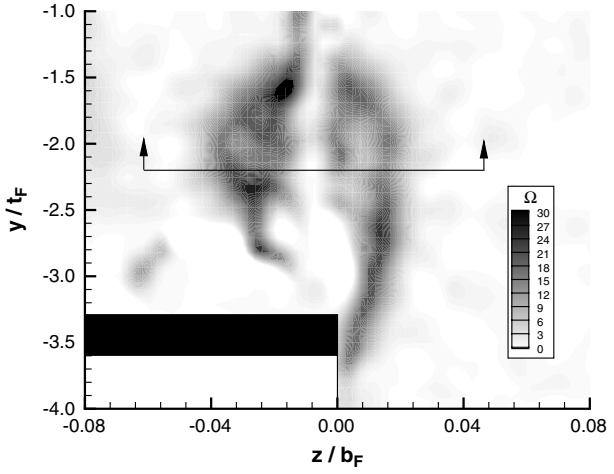

c) PIV plane 3 ($x_F/c_F = 0.9$)

Fig. 10 PIV data for the hard wall case (including profile locations).

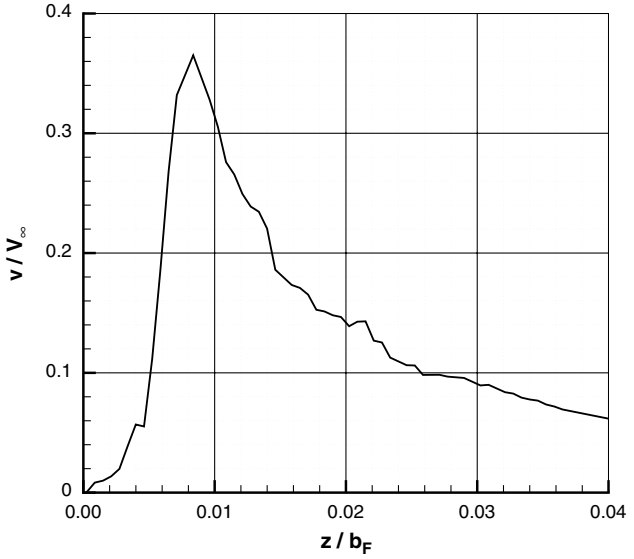

a) v profile at $y/t_F = -0.375$ at PIV plane 1

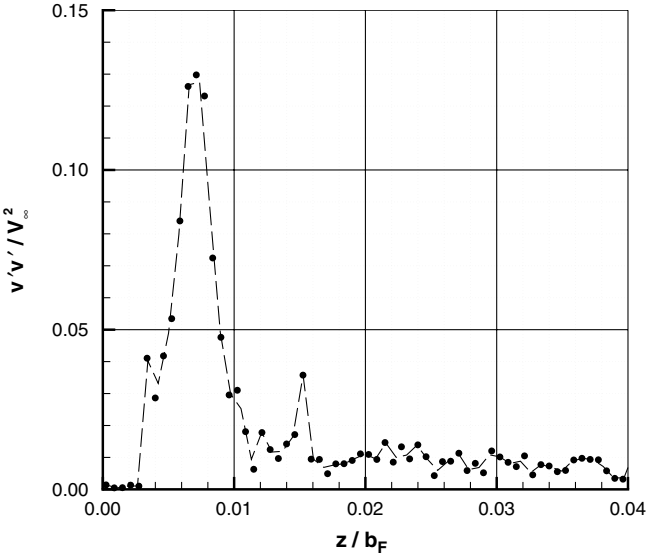

b) $v'v'$ profile at $y/t_F = -0.375$ at PIV plane 1

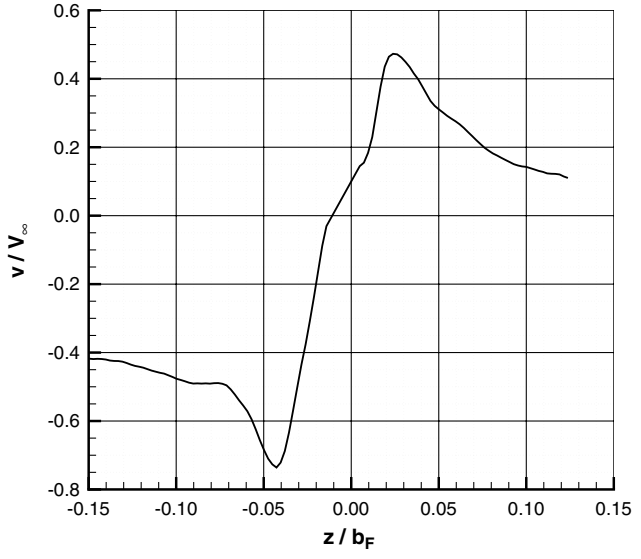

c) v profile at $y/t_F = -2.2$ at PIV plane 3

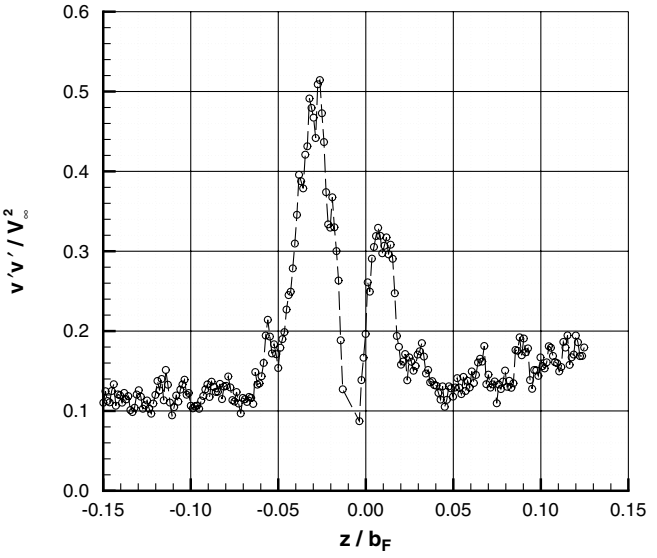

d) $v'v'$ profile at $y/t_F = -2.2$ at PIV plane 3

Fig. 11 Vortex profiles.

The vorticity at PIV plane 2, located at $x_F/c_F = 0.6$, is shown in Fig. 10b. At this plane, the two vortices merged to form a single vortex whose reattachment point was on the suction surface of the flap. The vortex grew in the streamwise direction, and the strength of vorticity in the shear layer increased. Because of the induced flowfield caused by the vortex, the main element wake vorticity was displaced away from the surface outboard, but it was brought closer to the flap suction surface inboard of the side edge. As the vortex grew in strength and separated from the flap surface, the main element wake vorticity was wrapped around the vortex and convected toward the solid surface of the flap.

Toward the trailing edge of the flap, the vortex was fully detached from the vortex surface. This was aft of the focal point seen in the oil flow visualization. The vorticity at PIV plane 3 ($x_F/c_F = 0.9$) is shown in Fig. 10c. The vortex exhibited significant unsteadiness and was constantly fed from the shear layer that originated from the lower surface of the flap side edge. The diplacement of the vortex core was likely caused by the unsteady flow originating upstream as proposed in Sen's model [6] (in this configuration the wake from the main element that was entrained in the vortex) and unsteadiness inherent in the vortex itself caused by cylindrical shear layer instabilities and streamwise vortex instabilities as proposed in Khorrami and Singer's linear stability analysis [29]. The pressure field induced by the unsteady off-surface vortex interacted with the flap suction surface and sharp side edges.

The v velocity profile at PIV plane 3 across the vortex is shown in Fig. 11c. This profile was taken at a flap thickness position of $y/t_F = -2.2$. The location of this profile corresponded to the peak velocities at the extremities of the vortex. The peak v velocity inboard of the flap was approximately 1.5 times greater than the peak velocity outboard of the flap side edge. The side-edge vortex was in a nonuniform pressure field with strong gradients. These pressure gradients induced accelerations in the radial velocity of the vortex as evidenced by the velocity profile in Fig. 11c.

The turbulent stresses contained within the vortex provided an indication of their potential strength as noise sources. The normal turbulent stress ($v'v'$) profile is shown in Fig. 11d. This stress term dominated over the other stress terms (i.e., $u'u'$ and $u'v'$). The turbulent fluctuations at $z/b_F = 0.01$ corresponded to the turbulent shear layer that was wrapped around the flap side-edge vortex. Inboard of the flap side edge, the shear layer was convected toward the flap suction surface. The peak turbulent fluctuations were at

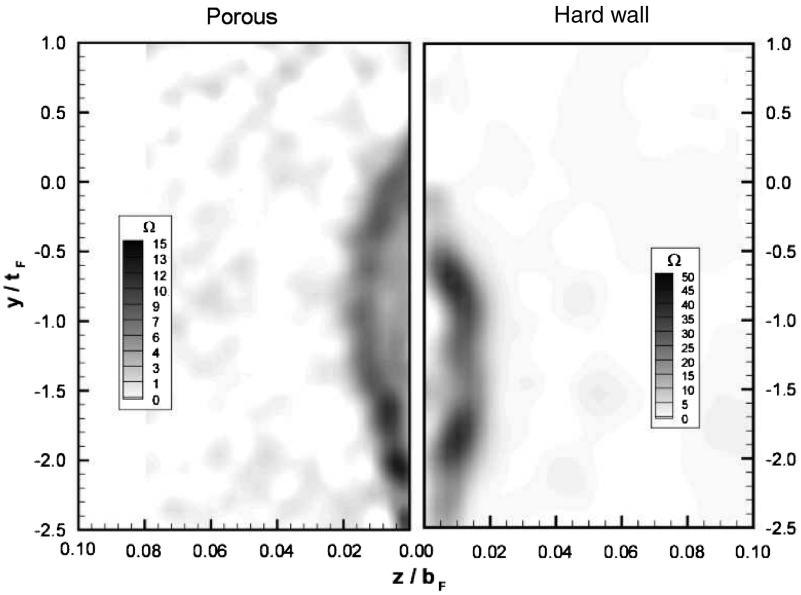

Fig. 12 Effect of porous flap side edge at PIV plane 2.

$z/b_F = -0.03$. The fluctuations at the edge of the flap side-edge vortex increased along the length of the shear layer as it was wrapped around the vortex. This nonuniform distribution of Reynolds stresses has important implications for noise generation at the flap side edge. Compared with the turbulent stress profile upstream at PIV plane 1 ($x_F/c_F = 0.2$), the magnitude of the turbulent stresses increased as the distance along the flap chord increased and the vortex grew.

2. Porous Side Edge

Figure 12 shows the nondimensional vorticity at PIV plane 2, located at $x_F/c_F = 0.6$, compared with the hard-wall case. A porous side edge of porosity 40 PPI and a relative density 10–12% was applied. It was difficult to obtain adequate PIV data near the surface due to reflections and diffraction of the laser light sheet from the open cell porous material due to its reticulated, cellular nature. However, the shear layer that was wrapped around the vortex and fed it with vorticity was captured. One effect of applying a porous side edge to the flap was a significantly weaker shear layer feeding the vortex and, hence, a weaker vortex. The magnitude of vorticity measured was significantly lower than the hard-wall case as shown in Fig. 12. The second effect was a displacement of the flap side-edge vortex vertically away from the flap surface. These two effects on the mean flowfield were determined also by Choudhari and Khorrami [13] in their computational study.

The velocity profiles at $z/b_F = 0.006$ are shown in Fig. 13a for both a hard-wall and a porous side edge. The vertical displacement of the edge of the vortex away from the flap surface was approximately one flap thickness (t_F) at this plane ($x_F/c_F = 0.6$). The peak spanwise velocities decreased significantly. This resulted in a decrease in the circulation strength of the vortex at this plane with the application of a porous side edge. This was due to the easing of the pressure difference between the suction and the pressure surfaces. The displacement effect can also be seen in the profile presented in Fig. 13a. The turbulent stress profile is shown in Fig. 13b toward the trailing edge of the flap at PIV plane 3. Again, the stress component $v'v'$ was dominant. The effect of the porous material was to reduce the magnitude of turbulent stresses in the shear layer that formed the side-edge vortex. This potentially reduced its strength as an acoustic source.

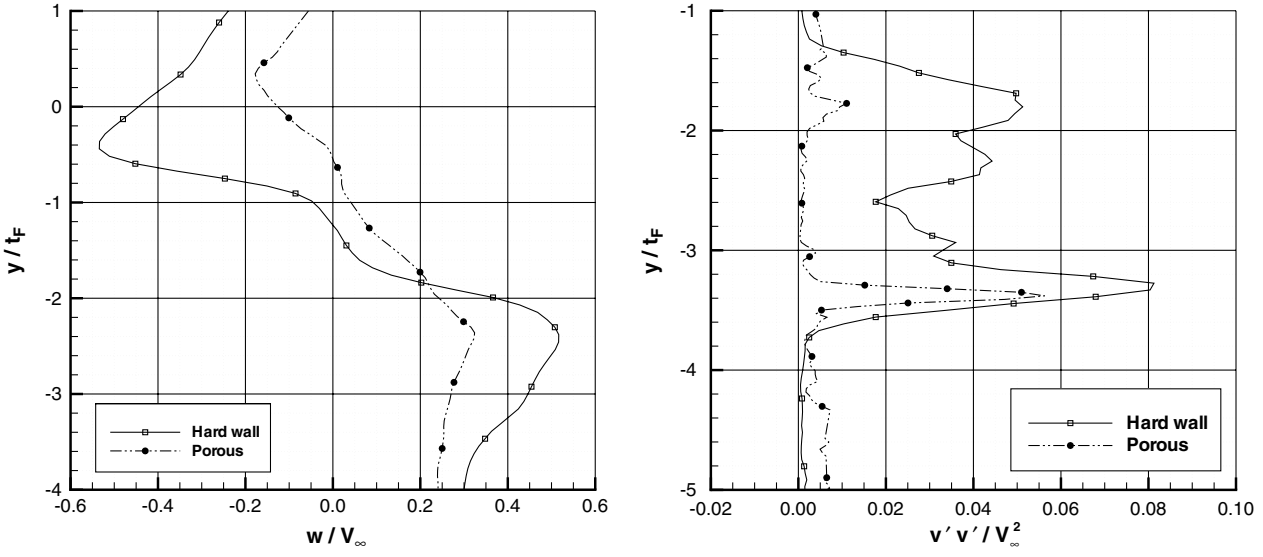

a) Comparison of velocity profiles with porous side-edge at z/b_F = 0.006 at PIV plane 2

b) Comparison of turbulent stress profile with porous side-edge at z/b_F = 0.006 at PIV plane 3

Fig. 13 Effect of porous side edge on near-field flow structures.

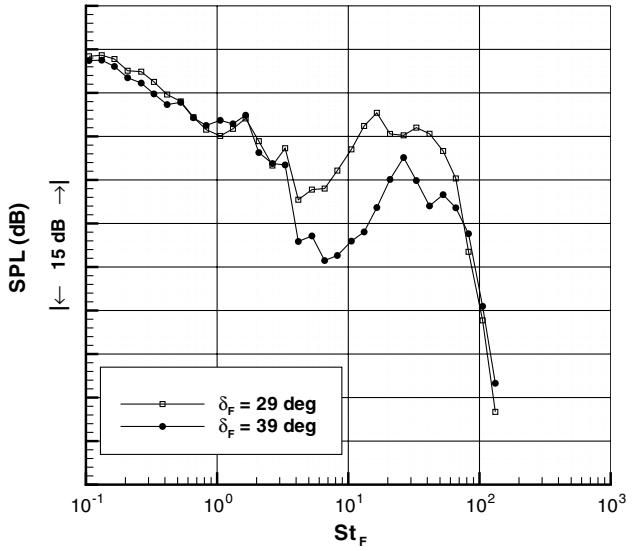

a) V_∞ = 30 m/s, α = 5 deg Mic 1

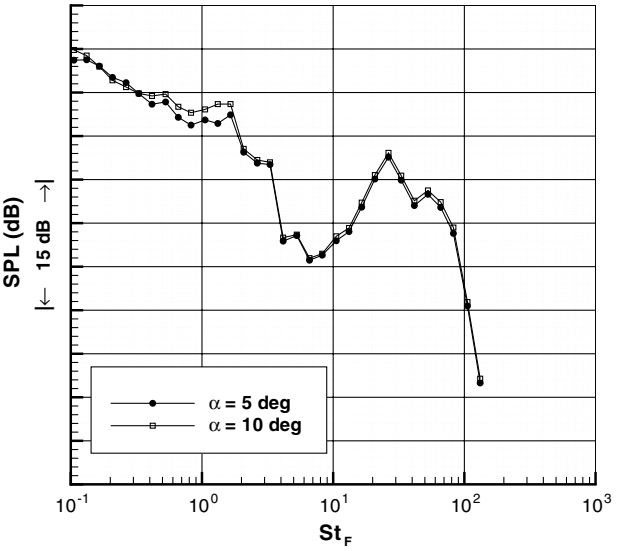

b) V_∞ = 30 m/s, δ_F = 39 deg Mic 1

Fig. 14 Microphone measurements for hard wall case.

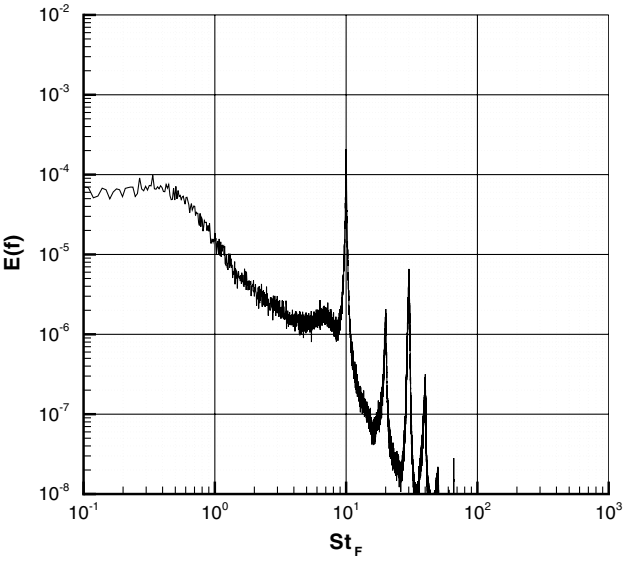

a) V_∞ = 10 m/s, α = 10 deg, δ_F = 29 deg

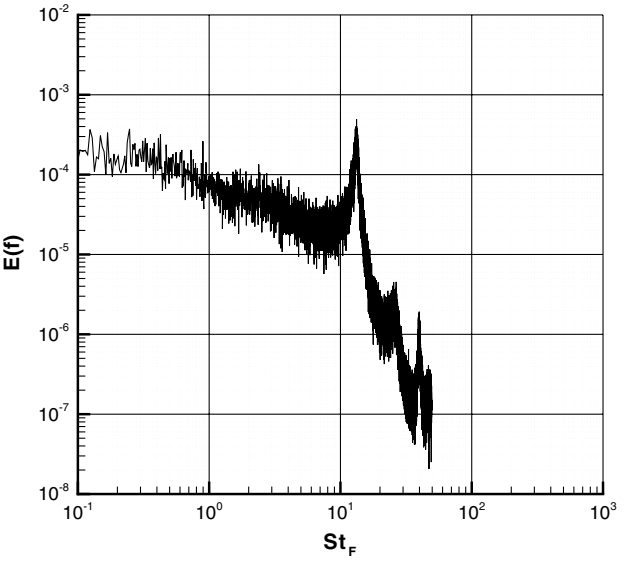

b) V_∞ = 20 m/s, α = 10 deg, δ_F = 29 deg

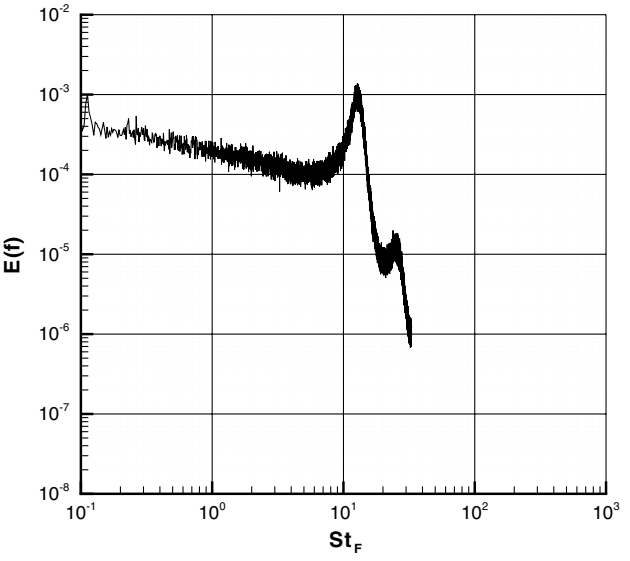

c) V_∞ = 30 m/s, α = 10 deg, δ_F = 29 deg

Fig. 15 Hot-wire measurements in the downstream vortex for hard-wall case.

In the vortex sound equation [30], the source term for vortex–surface interaction noise is a function of the cross product of the vorticity and velocity vectors (an appropriate Green's function is needed to take into account the influence of the body on how efficiently these sources generate sound [30]). Because of the impedance of the porous flap side edge and the weaker flap side-edge vortex, the convection velocity of the turbulent shear layer was retarded as shown in the PIV velocity profiles. The porous material also had the effect of reducing the magnitude of vorticity feeding the side-edge vortex and the turbulent stresses contained within the vortex. All these changes in the near-field aerodynamics reduced the efficiency of the noise source strength associated with the flap side-edge flowfield.

D. Spectral Content of Flowfield

1. Hard Wall

The on-surface pressure fluctuations at the flap side edge were determined by means of on-surface microphone measurements. A microphone was placed on the primary reattachment line on the side edge at a flap deflection degree of 29 deg as determined in the oil flow visualization at $x_F/c_F = 0.27$. The microphone was placed in a cartridge that held it in place flush against the flap surface. This allowed the unsteady pressures due to the impingement of the turbulent shear layer to be measured as discussed in the flowfield results. These spectral data from the microphones were averaged over one-third frequency bands.

The near-field pressures were measured at two different angles of attack (5 and 10 deg) and two flap deflection angles (29 and 39 deg). The near-field pressure fluctuations at the flap side edge were broadband in nature and were most prominent from a Strouhal number, based on flap chord, of 10 to 50. This is a similar value as quoted in other studies for the shear layer instabilities [7,12].

Changing the flap deflection angle shifted the primary reattachment line toward the suction surface of the flap so that the turbulent shear layer no longer directly impinged on the microphone location. This led to a decrease in the pressure fluctuations measured locally at this particular point as shown in Fig. 14a. Increasing the flap deflection angle also increased the dominant frequency of the peak from one-third frequencies of 2.5 kHz ($St_F = 16.5$) to 4 kHz ($St_F = 26.4$). Increasing the main element angle of attack (α) had a minimal effect on the near-field pressure fluctuations measured at the flap side edge as shown in Fig. 14b.

Hot-wire measurements made in the vortex core, at a coordinate position of (6,0.05,0), allowed the spectral content of the velocity fluctuations in the vortex to be determined. The results at an angle of attack of 10 deg and a flap deflection angle of 29 deg are shown in Fig. 15 for three different airspeeds. A feature centered around a

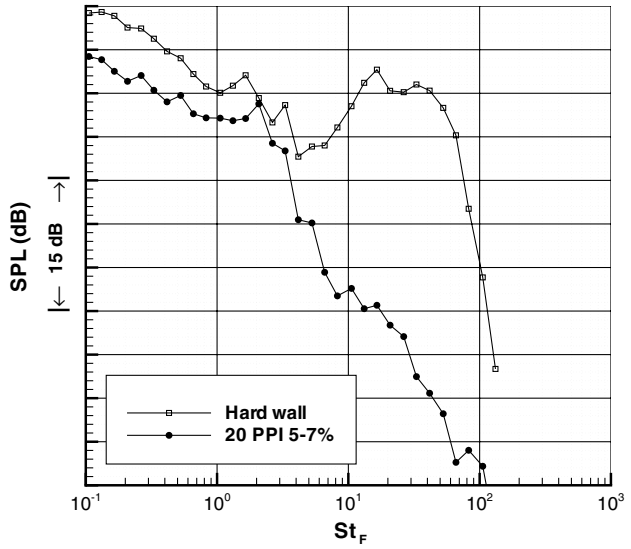

a) V_∞ = 30 m/s, α = 5 deg, δ_F = 29 deg 20 PPI 5-7%

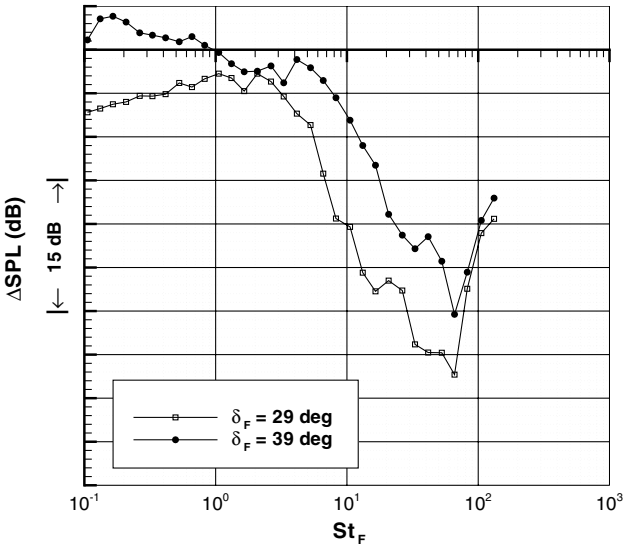

b) V_∞ = 30 m/s, α = 10 deg 20 PPI 5-7%

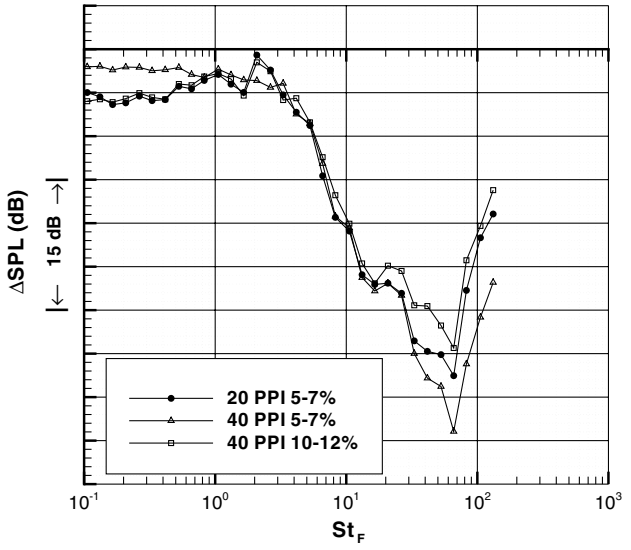

c) V_∞ = 30 m/s, α = 5 deg, δ_F = 29 deg

Fig. 16 On-surface microphone measurements for mic 1 with a porous side edge.

Strouhal number of 13.2 based on flap chord was measured at the two highest Reynolds numbers. At a Reynolds number of 0.7×10^6, the hot-wire spectrum in Fig. 15a showed a tonal peak at a Strouhal number of 10. As the Reynolds number increased to 1.4×10^6 and 2.0×10^6, the frequency of this peak increased to a Strouhal number of 13.2 at both Reynolds numbers. As the Reynolds number increased the bandwidth of the peak also increased, and it was no longer tonal in nature. This result showed the importance of the Reynolds number on the instabilities in the flap side-edge vortex. The spectra at $Re = O(10^5)$ contained a tonal feature at an incorrect frequency that was different at $Re = O(10^6)$. There was no evidence of the tonal peak at a Strouhal number of 6.0 that was determined by Dobrzynski et al. [24]. According to Dobrzynski et al. this tone was an artefact of laminar flow in scale model testing and did not appear in full-scale tests.

2. *Porous Side Edge*

The effect of applying a porous side edge on the pressure fluctuations in the near field was measured using on-surface microphones. Changes in the spectra with a porous side-edge treatment of 20 PPI 5–7% with angle of attack and flap deflection angle are discussed. These are generally applicable to all the porous treatments. Finally, the relative differences, where they existed, between the remaining two porous treatments and the 20 PPI 5–7% spectra are discussed.

The spectrum measured at microphone (mic) 1, at a freestream velocity of 30 m/s, an angle of attack of 5 deg, and a flap deflection angle of 29 deg, is shown in Fig. 16a. The major feature in the hard-wall measurements at these conditions was a large broadband hump centered around a Strouhal number of 16.5 (Fig. 14a). The effect of applying the porous treatment to the flap side edge was to remove this broadband hump almost completely. The location of mic 1 corresponded to the reattachment point of the primary shear layer on the flap side edge. The pressure fluctuations at this microphone were due to the turbulent shear layer that was wrapped around the side-edge vortex impinging on the solid surface. Because of the finite impedance effect of the porous material and the reduced vortex strength, the convected turbulence impinging on the solid surface was greatly reduced as was shown in the flowfield measurements in the previous section.

The change in near-field pressure fluctuation plots shown in Figs. 16b and 16c were produced by subtracting the one-third averaged hard-wall spectra from the one-third averaged porous spectra. The near-field pressure fluctuations at the flap side edge with the porous treatment were not sensitive to the angle of attack, similar to the hard-wall case. However, the spectra were sensitive to the flap deflection angle. The effect of increasing the flap deflection angle from 29 to 39 deg was to reduce the effectiveness of the porous flap side edge at all airspeeds and main element angles of attack (Fig. 16b). At 30 m/s this led to a near-field reduction in pressure fluctuations of 7 dB at a flap deflection angle of 29 deg. At a higher flap deflection angle both the vortex and the turbulent shear layer that fed the vortex were stronger. Therefore, the change in sound pressure level between the hard wall and porous side edge was less with the higher flap deflection angles.

The change in local pressure fluctuations at the flap side edge for all three porous materials is shown in Fig. 16c for a main element angle of attack of 5 deg and a flap deflection angle of 29 deg. The peak reduction with the porous material was centered around a Strouhal number of 60. This suggested that the finite impedance of the porous material was an important factor because acoustic absorption is a high-frequency phenomenon [15]. The major reductions in the near-field pressure fluctuations were from 2 to 12.5 kHz. The porous flap side-edge treatment of 40 PPI 5–7% produced the most reductions. However, at frequencies less than 200 Hz the magnitude of the reduction was less compared with the other two treatments. The least permeable of the treatments (40 PPI 10–12%) resulted in the smallest peak reduction. At frequencies less than 1 kHz the reduction is similar to the treatment with 20 PPI 5–7%.

The reductions measured were near-field pressure perturbations (both hydrodynamic and acoustic). Reductions in the far-field acoustics cannot be inferred from on-surface microphone measurements. However, the reductions in the near-field pressure perturbations were consistent with the near-field flowfield measurements that demonstrated a reduction in the turbulent stresses and a weaker vortex.

IV. Conclusions

The aerodynamic penalty associated with the use of a porous flap side edge was a very slight increase in drag. The magnitude of the loss in aerodynamic lift was comparable to the accuracy of the measurements. With the increase in drag the aerodynamic efficiency was reduced by 1.1% averaged over the angle of attack range tested. This was close to the repeatability of the measurements.

The PIV measurements detailed the peak turbulent stresses in the flap side-edge flowfield. These originated in the turbulent shear layer that formed the side-edge vortex. The magnitude of the turbulent stresses increased along the chord of the flap as the size of the vortex increased. The side-edge vortex also entrained the main element wake. By applying a porous side edge to the flap, the PIV measurements showed that the magnitude of vorticity in the shear layer wrapped around the vortex was reduced compared with that of the hard-wall case and that the side-edge vortex was displaced further away from the flap surface. Both these effects on the mean flowfield had been determined previously in computational work. The flowfield measurements also showed that the turbulent stresses in the shear layer were reduced with the application of a porous flap side edge as well as the convection velocity of the shear layer around the vortex. These changes in the aerodynamic flowfield suggested a weaker noise source at the flap side edge.

An on-surface microphone was placed on the point where the turbulent shear layer that separated from the pressure surface of the flap attached to the flap side edge. Midfrequency disturbances dominated the near field. An on-surface microphone, located at the primary vortex attachment line, showed a broadband hump, which dominated between a Strouhal number of 10 (1.4 kHz) and 50 (7.1 kHz), similar to previously reported values. The pressure fluctuations depended on flap deflection angle. A hot wire measuring velocity perturbations in the off-surface vortex measured instabilities in the vortex at a Strouhal number of 13.2. The effect of applying a porous flap side edge on the near-field pressure fluctuations measured at the primary reattachment line was to reduce them. This was consistent with the measurements that showed a reduced convection velocity of the shear layer and a reduction in the turbulent stresses. The effect of varying the resistance of the porous side edge was determined. There was a significant high-frequency reduction, which suggested that the acoustic impedance of the porous flap side edge was responsible for some of the reduction. It should be noted that far-field acoustic changes cannot be inferred from the near-field pressure fluctuations, although they were consistent with the expected changes brought about by the flowfield modifications.

The advantage of a porous material as a method of modifying the flowfield in the vicinity of a flap side edge is that it is a passive method with no additional energy requirements and an almost negligible aerodynamic penalty.

Acknowledgments

The research funding for this project was provided by Airbus. David Angland wishes to thank the School of Engineering Sciences, University of Southampton for providing a research studentship.

References

[1] Fink, M. R., and Schlinker, M. H., "Airframe Noise Component Interaction Studies," *Journal of Aircraft*, Vol. 17, No. 2, 1980, pp. 99–105. doi:10.2514/3.57880

[2] Ahyte, W. F., Miller, W. R., and Meecham, W. C., "Wing and Flap Noise Measured by Near- and Far-Field Cross-Correlation

Techniques," AIAA Paper 79-0667, 1979.
[3] Kendall, J. M., and Ahyte, W. F., "Noise Generation by a Lifting Wing/Flap Combination at Reynolds Numbers to 2.8×10^6," AIAA Paper 80-0035, 1980.
[4] Howe, M. S., "On the Generation of Side-Edge Flap Noise," *Journal of Sound and Vibration*, Vol. 80, No. 4, 1982, pp. 555–573. doi:10.1016/0022-460X(82)90498-9
[5] Hardin, J. C., "Noise Radiation from the Side-Edge of Flaps," *AIAA Journal*, Vol. 18, No. 5, 1980, pp. 549–552. doi:10.2514/3.7668
[6] Sen, R., "Vortex-Oscillation Model of Airfoil Side-Edge Noise," *AIAA Journal*, Vol. 35, No. 3, 1997, pp. 441–449. doi:10.2514/2.149
[7] Macaraeg, M. G., "Fundamental Investigations of Airframe Noise," AIAA Paper 98-2224, 1998.
[8] Meadows, K. R., Brooks, T. F., Humphreys, W. M., Hunter, W. W., and Gerhold, C. H., "Aeroacoustic Measurements of a Wing-Flap Configuration," AIAA Paper 97-1595, 1997.
[9] Brooks, T. F., and Humphreys, W. M., "Flap Edge Aeroacoustic Measurements and Predictions," AIAA Paper 2000-1975, 2000.
[10] Khorrami, M. R., Berkman, M. E., Li, F., and Singer, B. A., "Computational Simulations of a Three- Dimensional High-Lift Wing," AIAA Paper 2002-2804, 2002.
[11] Khorrami, M. R., Singer, B. A., and Radeztsky, R. H., "Reynolds-Averaged Navier–Stokes Computations of a Flap-Side-Edge Flowfield," *AIAA Journal*, Vol. 37, No. 1, 1999, pp. 14–22. doi:10.2514/2.687
[12] Street, C. L., "Numerical Simulation of a Flap-Edge Flowfield," AIAA Paper 98-2226, 1998.
[13] Choudhari, M., and Khorrami, M. R., "Computational Study of Porous Treatment for Altering Flap Side-Edge Flow Field," AIAA Paper 2003-3113, 2003.
[14] Chow, L. C., Mau, K., and Remy, H., "Landing Gear and High Lift Devices Airframes Noise Research," AIAA Paper 2002-2408, 2002.
[15] Revell, J. D., Kuntz, H. L., Balena, F. J., Horne, C., Storms, B. L., and Dougherty, R. P., "Trailing Edge Flap Noise Reduction by Porous Acoustic Treatment," AIAA Paper 97-1646, 1997.
[16] Storms, B. L., Hayes, J. A., Jaeger, S. M., and Soderman, P., "Aeroacoustic Study of Flap-Tip Noise Reduction Using Continuous Moldline Technology," AIAA Paper 2000-1976, 2000.
[17] Koop, L., and Ehrenfried, K., "Reduction of Flap Side Edge Noise: Passive and Active Flow Control," AIAA Paper 2004-2803, 2004.
[18] Storms, B. L., Takahashi, T. T., Horne, W. C., Ross, J. C., Dougherty, R. P., and Underbrink, J. R., "Flap Tip Treatments for the Reduction of Lift-Generated Noise," NASA CDTM-21006, 1996.
[19] Ross, J. C., Storms, B. L., and Kumagai, H., "Aircraft Flyover Noise Reduction Using Lower Surface Flap-Tip Fences," NASA CDTM-21004, 1995.
[20] Horne, C. F., Hayes, J., and Ross, J. C., "Measurements of Unsteady Pressure Fluctuations on the Surface of an Unswept Multi-Element Airfoil," AIAA Paper 97-1645, 1997.
[21] Blackner, A. M., and Davis, C. M., "Airframe Noise Source Identification Using Elliptical Mirror Measurement Techniques," *Proceedings of Inter-Noise 95*, 1995, pp. 203–206.
[22] Guo, Y. P., and Joshi, M. C., "Noise Characteristics of Aircraft High Lift Systems," *AIAA Journal*, Vol. 41, No. 7, 2003, pp. 1247–1256. doi:10.2514/2.2093
[23] Choudhari, M., Lockard, D. P., Macaraeg, M. G., Singer, B. A., Streett, C. L., Neubert, G. R., Stoker, R. W., Underbrink, J. R., Berkman, M. E., Khorrami, M. R., and Sadowski, S. S., "Aeroacoustic Experiments in the Langley Low-Turbulence Pressure Tunnel," NASA TM-2002-211432, 2002.
[24] Dobrzynski, W., Gehlhar, B., and Buchholz, H., "Model and Full Scale High-Lift Wing Wind Tunnel Experiments Dedicated to Airframe Noise Reduction," *Aerospace Science and Technology*, Vol. 5, No. 1, 2001, pp. 27–33. doi:10.1016/S1270-9638(00)01079-8
[25] Bear, J., *Dynamics of Fluids in Porous Media*, Dover, New York, 1972.
[26] "Duocel Aluminum Foam Brochure," ERG Materials and Aerospace Corp., Oakland, CA, 2006.
[27] Engineering Sciences Data Unit, *Blockage Corrections for Bluff Bodies in Confined Flows*, No. 80024, ESDU International, Ltd., London, 1998.
[28] McInerny, S. A., Meecham, W. C., and Soderman, P. T., "An Experimental Investigation of Wing Tip Turbulence with Applications to Aerosound," AIAA Paper 86-1918, 1986.
[29] Khorrami, M. R., and Singer, B. A., "Stability Analysis for Noise-Source Modeling of a Part-Span Flap," *AIAA Journal*, Vol. 37, No. 10, 1999, pp. 1206–1212. doi:10.2514/2.614
[30] Howe, M. S., *Theory of Vortex Sound*, Cambridge Univ. Press, New York, 1st ed., 2002.

F. Coton
Associate Editor